Assessment of Mechanical Properties of Tissue in Breast Cancer-Related Lymphedema Using Ultrasound Elastography

Hoda S. Hashemi, Stefanie Fallone, Mathieu Boily, Anna Towers, Robert D. Kilgour, and Hassan Rivaz

***Abstract*—Breast cancer-related lymphedema (BCRL) is a consequence of a malfunctioning lymphatic drainage system resulting from surgery or some other form of treatment. In the initial stages, minor and reversible increases in fluid volume of the arm are evident. As the stages progress over time, the underlying pathophysiology dramatically changes with an irreversible increase in arm volume most likely due to a chronic local inflammation leading to adipose tissue hypertrophy and fibrosis. Clinicians have subjective ways to stage the degree and severity such as the pitting test which entails manually comparing the elasticity of the affected and unaffected arms. Several imaging modalities can be used but ultrasound appears to be the most preferred because it is affordable, safe and portable. Unfortunately, ultrasonography is not typically used for staging lymphedema because the appearance of the affected and unaffected arms is similar in B-mode ultrasound images. However, novel ultrasound techniques have emerged, such as elastography that may be able to identify changes in mechanical properties of the tissue related to detection and staging of lymphedema. This paper presents a novel technique to compare the mechanical properties of the affected and unaffected arms using quasi-static ultrasound elastography to provide an objective alternative to the current subjective assessment. Elastography is based on Time Delay Estimation (TDE) from ultrasound images to infer displacement and mechanical properties of the tissue. We further introduce a novel method for TDE by incorporating higher-order derivatives of the ultrasound data into a cost function, and propose a novel optimization approach to efficiently minimize the cost function. This method works reliably with our challenging patient data. We collected Radio-Frequency (RF) ultrasound data from both arms of seven patients with Stage 2 lymphedema, at six different locations in each arm. The ratio of strain in skin, subcutaneous fat and skeletal muscle divided by strain in the standoff gel pad was calculated in the unaffected and affected arms. The p-values using a Wilcoxon sign-rank test for the skin, subcutaneous fat, and skeletal muscle were 1.24×10^{-5}, 1.77×10^{-8}, 8.11×10^{-7} respectively, showing differences between the unaffected and affected arms with a very high level of significance.**

H. S. Hashemi is with the Department of Electrical and Computer Engineering, University of British Columbia, V6T 1Z4, BC, Canada

S. Fallone and R. D. Kilgour are with the Department of Exercise Science, Concordia University, Montreal, QC, H3G 1M8, Canada

M. Boily is with the Department of Radiology, McGill University Health Centre (MUHC), Montreal, QC, H4A 3J1, Canada

A. Towers is the the Director of the Lymphedema program at the Department of Oncology, McGill University, Montreal, QC, H4A 3J1, Canada

A. Towers and R. D. Kilgour are with the McGill Nutrition and Performance Laboratory, Montreal, QC, H4A 3J1, Canada

H. Rivaz and R.D. Kilgour are PERFORM Centre researchers, Concordia University, Montreal, QC, H3G 1M8, Canada

H. Rivaz is with the Department of Electrical and Computer Engineering, Concordia University, Montreal, QC, H3G 1M8, Canada

Email: H. S. Hashemi: hoda@ece.ubc.ca

Email: H. Rivaz: hrivaz@ece.concordia.ca

***Index Terms*—Breast Cancer, Lymphedema, Quasi-Static Ultrasound Elastography, Time Delay Estimation, TDE, Efficient Second-Order Minimization.**

I. Introduction

Breast cancer related lymphedema (BCRL) is manifested by a noticeable increase in excess arm volume due to treatment (e.g., surgery, radiation therapy) effects on the functioning of the lymphatic fluid drainage system [1]. This swelling can occur soon after treatment or may take several years to develop [2]. Regardless of its time to appearance, BCRL typically progresses through several clinical stages (Stages 0-3) with the initial stages (Stages 0-1) characterized by mild fluid accumulation that can be reversed by simply elevating the arm [3]. However, the successive stages (Stages 2-3) are defined by irreversible swelling that is not totally related to fluid accumulation but to suspected changes in tissue morphology of the arm such as in the skin, subcutaneous fat, and skeletal muscle. These tissue adaptations may be directly related to an abnormal pathophysiology resulting in localized inflammation of the arm leading to adipose tissue hypertrophy and pathological fibrotic changes [1]. Clearly, a shift in staging from Stage 0-1 to Stage 2-3 represents a significant change in the clinical course of this condition and warrants future investigation into the ways in which BCRL is detected and staged.

Currently, BCRL staging consists of a simple subjective assessment procedure involving an assessment of tissue pitting. Using this method, if the skin becomes "pitted" after applying finger pressure to the area, then the patient is categorized into a certain stage. This technique lacks precision and a vision of what is happening beneath the level of the skin. Thus, more sophisticated methods must be explored. There are imaging modalities that have been used in the past to detect lymphedema including magnetic resonance imaging (MRI), computed tomography (CT), and ultrasonography [3]–[7]. While MRI and CT show structural changes to tissues, their clinical utility is limited due to their considerable cost and limited availability. On the other hand, ultrasound can provide real-time measures, is portable and does not emit radiation. Furthermore, recent advances in ultrasonography such as elastography may help better assess mechanical properties of the skin, subcutaneous fat and skeletal muscle of the arm and to aid the clinician in staging lymphedema based upon changes in tissue morphology.

Ultrasound imaging can be used to investigate changes in the subcutaneous tissue that are associated with lymphedema,

which include increased thickness of the dermis, a shift from hypo- to hyperechogenicity of the subcutis, and fluid retention located in the dermis, interlobular space, and superficial fascia [8]–[10]. However, ultrasonic appearance of these changes can be negligible and hard to detect.

Certain ultrasound-based techniques have been used to tackle these problems. Poroelastographic techniques are employed to explore changes in mechanical properties of the tissue [11]–[13]. Recent work has also applied compression with the ultrasound probe, and measured the thickness of the skin and subcutis in the upper extremity [14]–[17]. These studies show that skin thickness and subcutis layers are different in the unaffected versus affected arms. However, these methods use B-mode ultrasound to manually measure tissue thickness. This measurement can be performed with greater accuracy by using Radio-Frequency (RF) data instead of B-mode images, and by using Time Delay Estimation (TDE) methods that are widely used in ultrasound elastography [18]–[25]. Such automatic TDE estimation will also be less time consuming and less subjective than manually measuring tissue thickness. Another difficulty in manually measuring skin thickness lies in normalization of the applied pressure. When comparing the thickness of the two arms, the applied pressure should be equal. Therefore, new research has proposed to use pressure sensors to generate equal pressure in both arms [26]. In this work, we propose an alternative approach wherein we use an acoustic gel pad to normalize the applied pressure on the tissue. In addition to normalizing the applied pressure, the gel pad will increase the quality of the ultrasound data at the skin.

TDE from RF data is a challenging task that is the heart of almost all ultrasound elastography methods, and as such, is an active field of research. The most common approach divides the RF data in one of the images into (usually overlapping) windows, and performs TDE by finding the best corresponding window in the other image using either intensity or phase of the RF data [27]–[29]. The second class uses optimization techniques to calculate a displacement field [30]–[34]. In addition to its wide application in almost all elastography methods, TDE has many applications such as segmentation [35] and motion compensation [36]. Our group has developed several techniques in the second class, which are usually less susceptible to decorrelation noise compared to the window-based methods [37].

Herein, we calculate TDE from the RF signal using a novel method, and estimate strain values for the gel pad, skin, subcutaneous fat, and skeletal muscle layers in the affected and unaffected arms. We use the strain values to study differences between the two arms. To the best of our knowledge, this is the first time that this approach is used in studying the differences in different layers of subcutaneous tissues between the affected and unaffected arms. More specifically, the contributions of this work are:

1) Introducing a novel method based on ultrasound elastography for comparing affected and unaffected arms in patients with lymphedema.
2) Proposing a novel method for TDE of quasi-static elastography that works reliably with the challenging patient data.

The new technique for estimation of the displacement map between two frames of RF data is based on minimization of a regularized cost function that has two terms of data similarity and continuity of TDE. It is based on our recent work entitled GLobal Ultrasound Elastography (GLUE) [38]. We introduce two novel techniques to improve GLUE. First, second-order Taylor expansion is used in the cost function, compared to first-order Taylor expansion used in GLUE. We show that inclusion of second-order Taylor terms makes the optimization problem intractable, and therefore propose a novel method for linearizing the cost function. Second, we utilize Efficient Second-order Minimization (ESM), an optimization technique that is widely shown to have superior convergence properties in computer vision and image registration [39]–[41]. We call our new method GLUE2, and show using simulation and phantom experiments that it outperforms GLUE. To focus the clinical results on differences between the mechanical properties of the unaffected and affected arms, we only present the results of GLUE2. More detailed comparisons of GLUE and GLUE2 is provided in the Supplementary Material.

To improve the quality of the superficial tissue and to normalize the compression applied to the arm during elastography, we use a gel pad, which does not contain any scatterers and appears dark in ultrasound images. It is important to measure the strain in the gel pad to normalize the manual compression, which unfortunately is not straightforward using window-based methods. To solve this problem, previous work has proposed post-processing steps to fill-in these dark regions [42]. However, both GLUE and GLUE2 are able to reliably calculate the displacement field in the gel pad since they automatically rely on the regularization term if no data term is available. Therefore, in addition to providing high-quality strain images, our proposed method is ideally suited for staging lymphedema.

A much shorter version of this work is recently published in a conference [43]. The differences are as follows. First, the introduction and literature review of this paper are more comprehensive. Second, this paper includes results of finite element and Field II simulations as well as data from seven patients, whereas the conference paper did not include simulation results and was further limited to two patients only. And last, the results are discussed in substantial more detail in this extended paper.

II. Methods

In this section, we first briefly describe the closely related previous work of GLUE [38]. We then present GLUE2.

A. GLobal Ultrasound Elastography (GLUE)

Let I_1 and I_2 be images of size $m \times n$ that correspond to images obtained before and after some deformation. Also, let $a_{i,j}$ and $l_{i,j}$ denote be axial and lateral displacements of sample (i, j), where $i = 1 \cdots m$ and $j = 1 \cdots n$. First, an estimate of the displacement field in the axial ($a_{i,j}$) and lateral ($l_{i,j}$) directions are calculated using the Dynamic Programming Analytic Minimization (DPAM) method [44]. DPAM calculates TDE by optimization of a cost function that incorporates both

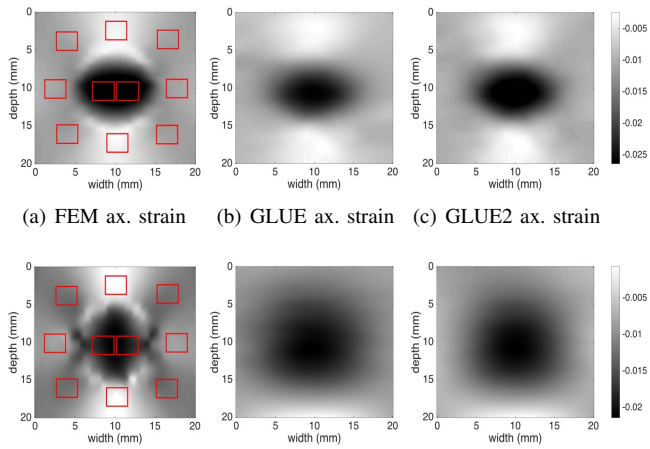

(a) FEM ax. strain (b) GLUE ax. strain (c) GLUE2 ax. strain

(d) FEM lat. strain (e) GLUE lat. strain (f) GLUE2 lat. strain

Fig. 1. Results of the Field II and Finite Element Method (FEM) simulation experiment. (a)-(c) show axial strains corresponding to respectively ground truth, GLUE and GLUE2. (d)-(f) show lateral strains corresponding to respectively ground truth, GLUE and GLUE2. The red windows in (a) and (d) are used for SNR and CNR calculations.

amplitude similarity and displacement continuity. The simultaneous estimation is performed for individual RF-lines, limiting the algorithm to utilize only a small fraction of the information available from the entire image in every optimization. The goal of GLUE is to find subsample $\Delta a_{i,j}$ and $\Delta l_{i,j}$ displacements such that the duple $(a_{i,j} + \Delta a_{i,j}, l_{i,j} + \Delta l_{i,j})$ which refines DPAM estimates $(a_{i,j}, l_{i,j})$ and provides more accurate axial and lateral displacement estimates for all the samples of the RF frame simultaneously. The GLUE cost function is defined as:

$$C(\Delta a_{1,1}, \cdots, \Delta a_{m,n}, \Delta l_{1,1}, \cdots, \Delta l_{m,n}) = \sum_{j=1}^{n} \sum_{i=1}^{m} \{D(i,j) + R(i,j)\} \tag{1}$$

where the data term D is:

$$D(i,j) = [I_1(i,j) - I_2(i + a_{i,j} + \Delta a_{i,j}, j + l_{i,j} + \Delta l_{i,j})]^2, \tag{2}$$

and the regularization term R is:

$$\begin{aligned} R = & \\ & \alpha_1(a_{i,j} + \Delta a_{i,j} - a_{i-1,j} - \Delta a_{i-1,j})^2 \\ & + \beta_1(l_{i,j} + \Delta l_{i,j} - l_{i-1,j} - \Delta l_{i-1,j})^2 \\ & + \alpha_2(a_{i,j} + \Delta a_{i,j} - a_{i,j-1} - \Delta a_{i,j-1})^2 \\ & + \beta_2(l_{i,j} + \Delta l_{i,j} - l_{i,j-1} - \Delta l_{i,j-1})^2, \end{aligned} \tag{3}$$

and α and β are regularization weights in axial and lateral directions respectively. The first-order 2D Taylor expansion around $(i + a_{i,j}, j + l_{i,j})$ gives:

$$I_1(i,j) - I_2(i + a_{i,j} + \Delta a_{i,j}, j + l_{i,j} + \Delta l_{i,j}) \approx I_1(i,j) - I_2(i + a_{i,j}, j + l_{i,j}) - I'_{2,a}\Delta a_{i,j} - I'_{2,l}\Delta l_{i,j}. \tag{4}$$

where $I'_{2,a}$ and $I'_{2,l}$ are the derivatives of the I_2 at the point $(i + a_{i,j}, j + l_{i,j})$ in the axial and lateral directions. Inserting Eq. 4 in Eq. 1 will make the cost function quadratic with respect to variables $\Delta a_{i,j}$ and $\Delta l_{i,j}$, and therefore can be efficiently optimized by setting its derivative to zero.

Fig. 2. CIRS phantom and the acoustic gel pad.

B. Incorporation of the Second-Order Taylor Expansion into the Cost Function

Minimizing the cost function provides us the displacement map. GLUE uses the first order Taylor expansion (Eq. 4) to approximate the nonlinear data term of cost function with a linear term. Including higher order derivatives of Taylor expansion reduces the error in the estimated data term. As a result, having more accurate cost function by including higher order derivatives for the data term can improve the accuracy of displacement estimation. However, doing so will make the derivative of Eq. 1 nonlinear, and therefore the optimization problem becomes intractable given that this equation typically has millions of variables. For example, an RF frame of size 1000 x 500 has a total of 500,000 samples. Each sample Eq. 1 results in two variables (i.e. the axial and lateral displacements). Therefore, the cost function in this case has 1 million variables.

We therefore propose a novel technique to incorporate the second-order Taylor expansion into the cost function while keeping the problem computationally efficient. Our proposed cost function is:

$$C = \sum_{j=1}^{n} \sum_{i=1}^{m} \{w(i,j)D(i,j) + R(i,j)\} \tag{5}$$

where w is the weight of each data term:

$$w(i,j) = \frac{1}{\epsilon + |I''(i,j)_{2,a}| + |I''(i,j)_{2,l}|} \tag{6}$$

where ϵ is a small positive constant to prevent the denominator from becoming zero, and $|I"_{2,a}|$ and $|I"_{2,l}|$ are the absolute values of second-order derivatives in the axial and lateral directions respectively. The weight w reduces the contribution of regions of the RF-data with high second-order derivatives where Eq. 4 does not hold. Therefore, this method utilizes second-order derivatives while keeping the cost function quadratic and tractable. This idea has some similarities to a previous work that utilized areas of the images wherein cost functions approximations are more accurate [45].

C. Efficient Second-order Minimization (ESM)

We also utilize the Efficient Second-order Minimization (ESM) optimization method [39] for the first time for TDE. ESM is shown to have superior convergence properties [40],

[41], [46] compared to the asymmetric Gauss-Newton optimization method used in GLUE.

Let $p = (i + a_{i,j}, j + l_{i,j})$ denote a vector containing the coordinate of a pixel after an approximate displacement $(a_{i,j}, l_{i,j})$, and consider $p + \Delta p = (i + a_{i,j} + \Delta a_{i,j}, j + l_{i,j} + \Delta l_{i,j})$ as its refined location after a small displacement estimate $(\Delta a_{i,j}, \Delta l_{i,j})$. ESM uses the following Taylor expansion to linearize the data term [39]:

$$I_2(p + \Delta p) = I_2(p) + \tfrac{1}{2}\{I'_{2,a}(p) + I'_{1,a}(p)\}\Delta a_{i,j} + \tfrac{1}{2}\{I'_{2,l}(p) + I'_{1,l}(p)\}\Delta l_{i,j} \tag{7}$$

Utilizing Eq. 7 in our cost function of Eq. 5, we have:

$$C(\Delta a_{1,1}, \cdots, \Delta a_{m,n}, \Delta l_{1,1}, \cdots, \Delta l_{m,n}) = \sum_{j=1}^{n}\sum_{i=1}^{m}\{w(i,j)[I_1(i,j) - I_2(i + a_{i,j}, j + l_{i,j}) - \tfrac{1}{2}(I'_{2,a}(p) + I'_{1,a}(p))\Delta a_{i,j} - \tfrac{1}{2}(I'_{2,l}(p) + I'_{1,l}(p))\Delta l_{i,j}]^2 + R(i,j)\} \tag{8}$$

where $I'_{1,a}$, $I'_{2,a}$, $I'_{1,l}$ and $I'_{2,l}$ are calculated at the point $(i + a_{i,j}, j + l_{i,j})$. This equation is a quadratic equation with respect to the unknowns $\Delta a_{i,j}$ and $\Delta l_{i,j}$, and therefore can be efficiently optimized by setting its derivative with respect to the unknowns to zero. ESM (Eq. 7) uses the derivatives of both images i.e. $I'_2(p) = \frac{1}{2}(I'_2(p) + I'_1(p))$. This equation can be utilized in both axial and lateral directions. By taking derivatives from this equation and obtaining $I"_2(p)$ in both axial and lateral directions, we modify the weight of the data (Eq. 6) term as follows:

$$w(i,j) = \frac{1}{\epsilon + \frac{1}{2}|I"(i,j)_{2,a} + I"(i,j)_{1,a}| + \frac{1}{2}|I"(i,j)_{2,l} + I"(i,j)_{1,l}|} \tag{9}$$

Once the displacement field is estimated, it is common to estimate its spatial gradient to generate strain images. We consider several displacement measurements and perform a least square regression to calculate the strain image [47]. Generally, large kernels are used to reduce noise amplification of the derivative operator. They generate smooth strain fields, but make the boundary of two different types of tissue blurred. In this work, the window length of 93 is used for differentiable kernel to strike a balance between smoothness and contrast of the strain image. Note that GLUE and GLUE2 estimate displacements for all samples of RF data, and therefore, 93 is the number of samples in the RF data and not number of windows typically used in popular window-based TDE methods.

The results are not sensitive to the values of the parameters. A good combination of the tuneable parameters of the GLUE2 technique are set to $\alpha_1 = 0.2$, $\alpha_2 = 0.1$, $\beta_1 = 0.2$, and $\beta_2 = 0.1$. The parameter ϵ is set to 0.07 in simulations, 0.8 for phantom experiment and 0.012 for the *in-vivo* patient data. Higher values of this parameter are more suitable for homogenous tissues, whereas lower values are more suitable in layered inhomogenous tissues discussed in Section IV. Changing the value of ϵ by 100% for the patient data will change the CNR and SNR values in the strain map by less than only 2%. Therefore, the results are not sensitive to the value of this parameter. For the parameters of the DPAM method we set $\alpha_{DP} = 0.15$, $\alpha = 5$, $\beta = 1$, and $\gamma = 0.005$. Ultrasound machines usually have presets for different organs (breast, thyroid, prostate, transcranial, etc.) for optimized imaging. The aforementioned parameters can be stored alongside these imaging presets in a commercial implementation of GLUE2.

GLUE2 is implemented in MATLAB, and our current implementation takes approximately 0.8 sec to run on a 4th generation 3.6 GHz Intel Core i7 for two RF frames of size 1000×100 to generate a 2D displacement map of the same size. The code can be optimized by implementing it in C++, and also by parallelism and use of GPU to run in real-time.

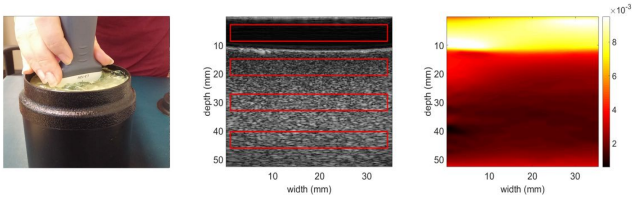

(a) CIRS phantom (b) B-mode image (c) GLUE2 Axial strain

Fig. 3. B-mode image and axial strain obtained from the ultrasound probe placement on the gel pad. CIRS elastography phantom and the ultrasound B-mode image are shown in (a) and (b). The axial strain obtained from GLUE2 is depicted in (c). The red windows in (b) are used for calculation of SNR and CNR.

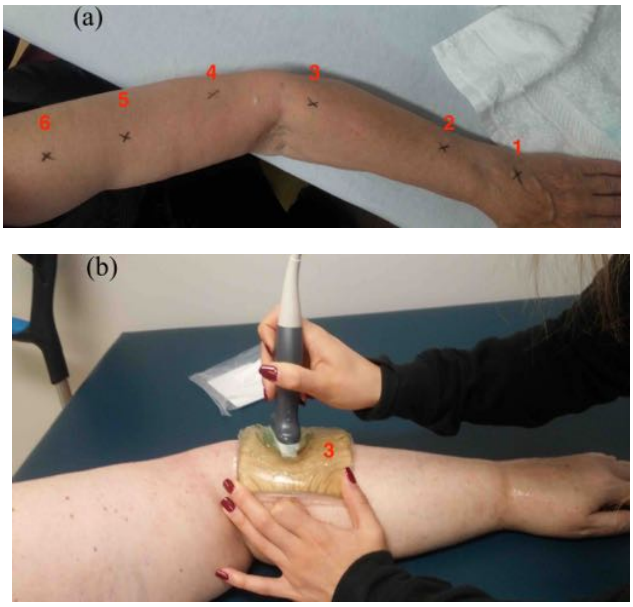

Fig. 4. Data collection from patients. (a) shows the six skin landmarks where ultrasound data collection was performed, and (b) shows RF data collection from an arm affected with lymphedema.

D. Simulation and Experimental Data

Simulation, phantom and *in-vivo* data from seven patients with stage 2 lymphedema are used to validate the performance of our proposed method. The simulated ultrasound images are generated using Field II [48], and ABAQUS (Providence, RI) Finite Element Method (FEM) software packages. We distribute more than 10 scatterers per cubic mm in the simulated

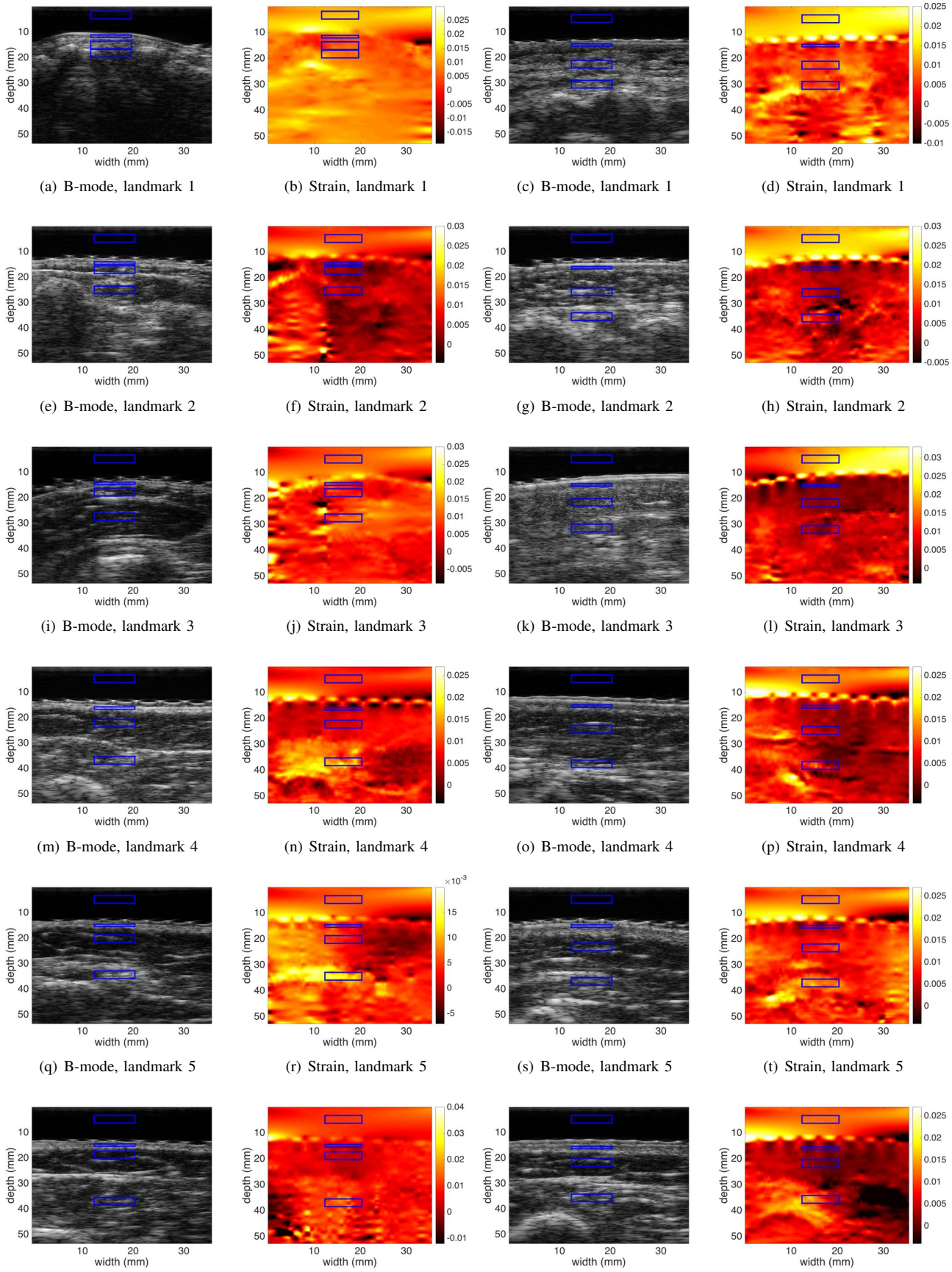

(a) B-mode, landmark 1 (b) Strain, landmark 1 (c) B-mode, landmark 1 (d) Strain, landmark 1

(e) B-mode, landmark 2 (f) Strain, landmark 2 (g) B-mode, landmark 2 (h) Strain, landmark 2

(i) B-mode, landmark 3 (j) Strain, landmark 3 (k) B-mode, landmark 3 (l) Strain, landmark 3

(m) B-mode, landmark 4 (n) Strain, landmark 4 (o) B-mode, landmark 4 (p) Strain, landmark 4

(q) B-mode, landmark 5 (r) Strain, landmark 5 (s) B-mode, landmark 5 (t) Strain, landmark 5

(u) B-mode, landmark 6 (v) Strain, landmark 6 (w) B-mode, landmark 6 (x) Strain, landmark 6

Fig. 5. Ultrasound and strain images of the 6 landmarks shown in Figure 4 in the unaffected arm (first and second columns) and affected arm (third and fourth columns).

phantom [49], and mesh the phantom for FEM analysis. We then displace the mesh nodes using the FEM package and calculate the displacement of each scatterer through interpolation of the neighboring nodes.

In phantom and *in-vivo* data collections, RF data was collected with an Alpinion E-Cube system (Bothell, WA) using the L3-12H transducer at the centre frequency of 10 MHz and the sampling rate of 40 MHz. The patient data were collected at the McGill University Health Centre (MUHC) Lymphedema clinic. Ethics approval was obtained from MUHC, and all subjects provided written consent to participate in this study. In all phantom and *in-vivo* experiments, the ultrasound probe was hand-held and was used to compress the tissue.

E. Normalization of the Compression Level Using Strain Ratio

According to the Hooke's law for linear elastic materials, $S = \frac{F}{A.E}$, where S is the strain, F is the perpendicular force, A is the area, and E is the Young's modulus. Note that according to this equation, increasing the force increases the strain, and therefore strain values from different experiments cannot be compared since the force can vary. However, assuming that the gel pad is linear elastic and that the applied force varies slowly so that viscous damping can be ignored, the force in the gel pad is equal to the force applied to the tissue, and therefore, dividing the strains by the strain in the gel pad allows comparison of strain values under different forces. We validate this theoretical prediction through real phantom experiments. To this end, we use the unit-less metric strain ratio (SR) to quantitatively compare the results of the affected and unaffected limb in patient data. SR is calculated for the skin, subcutaneous fat and skeletal muscle tissue using the following equations:

$$\mathrm{SR_s} = \frac{\bar{S_s}}{\bar{S_g}},\ \mathrm{SR_f} = \frac{\bar{S_f}}{\bar{S_g}},\ \mathrm{SR_m} = \frac{\bar{S_m}}{\bar{S_g}} \tag{10}$$

where $\bar{S_g}$, $\bar{S_s}$, $\bar{S_f}$ and $\bar{S_m}$ are the spatial average of the strain in the gel pad, skin, subcutaneous fat and skeletal muscle. All the spatial average values are calculated within a window of size 8mm×3mm in the corresponding regions of the strain image except for the skin which has less thickness and the window of size 8mm×1mm is used in calculations.

III. Results

This section includes results on simulation and phantom data, as well as results on women who are suffering from BCRL. The unitless metrics signal to noise ratio (SNR) and contrast to noise ratio (CNR) [50] are used to quantitatively assess the quality of strain images:

$$\mathrm{CNR} = \frac{C}{N} = \sqrt{\frac{2(\bar{s_t} - \bar{s_b})^2}{\sigma_t^2 + \sigma_b^2}},\ \mathrm{SNR} = \frac{\bar{s_t}}{\sigma_t} \tag{11}$$

where $\bar{s_b}$ and $\bar{s_t}$ are the spatial strain average of the background and target windows, and σ_b^2 and σ_t^2 are the spatial strain variance of the background and target windows.

A. Simulation Results

The strain images are calculated from the displacement fields obtained from GLUE and GLUE2 and are shown in Figure 1. These images, especially at the lesion boundaries, show that GLUE2 provides strain images that are sharper and have more contrast which makes it easier to distinguish the lesion from background. SNR and CNR values calculated using the background windows in Figure 1 (a) and (d) are reported in the Supplementary Material. These results show that GLUE2 improves the CNR in the axial strain from 18.15 to 52.74, i.e. a 190% improvement.

B. Phantom Results

For experimental validation, RF data is acquired from a CIRS elastography phantom (Norfolk, VA) with a Young's Elasticity Modulus of 7KPa as shown in Figure 2. The results are shown in Figure 3. (a) and (b) show the phantom and B-mode image respectively. The phantom is a uniform tissue which leads to an approximately uniform strain depicted in (c) for GLUE2. Unlike the simulation experiment, this phantom is uniform, and hence, it is hard to visually compare the results of GLUE and GLUE2. For this reason, and to keep the paper concise, we do not visually compare GLUE and GLUE2 and only compare them quantitatively. The SNR and CNR are calculated for 3 regions using the windows shown in (b). Please refer to Supplementary Material for the CNR and SNR measurments. The proposed method has 28% and 24% improvements in terms of CNR and SNR over the previous technique, GLUE.

To illustrate the advantage of SR over strain values, we compare their values in the phantom study at four different strain levels using GLUE2 (Table I). Basically, the strain values will increase if the applied pressure on the tissue is intensified. It causes problems for comparison of the strain values between two different ultrasound images for affected and unaffected arms because when sonographers take ultrasound images from patients, the applied force on the tissue is different for every ultrasound image. We therefore normalize the strain values of the tissue within an image against the strain values of the gel pad. This normalization makes the strain values less dependent to the applied pressure. In Table I, $\bar{S_p}$ are the average values of the strain in the phantom, which change substantially from 0.07% to 0.38% at different compression levels (an increase of 443%) as expected. However, SR values depict a much slower increase from 0.27 to 0.33 (an increase of only 22%). Note that theoretically, SR should not change at all and the small changes are likely caused by nonlinearities in mechanical properties of the gel pad or phantom. Therefore, SR can be used to reduce the impact of different levels of compression.

C. Patient Data

The study population was composed of women with Stage 2 breast cancer-related lymphedema. All participants in this study had a Body Mass Index (BMI) greater than 24 kg/m^2 and ranged in age from 54 to 81 years old. All the patients underwent breast cancer surgery and treatment more than 6 years ago. We placed the 6 following landmarks on both arms to mark the location of the data collection (Figure 4):

TABLE I
COMPARISON OF STRAIN AND SR AT 4 DIFFERENT COMPRESSION LEVELS. THE 443% INCREASE IN PHANTOM STRAIN $\bar{S}_p$ (FROM 0.07% TO 0.38%) IS SUBSTANTIALLY REDUCED TO 22% INCREASE IN SR (FROM 0.27 TO 0.33).

Compression level	$\bar{S}_p, \%$	SR
1	0.07	0.27
2	0.18	0.30
3	0.29	0.31
4	0.38	0.33

(a) 20% of the distance between the styloid process of the 5th digit and tip of it
(b) 20% of the distance between the styloid process of the 5th digit and olecranon
(c) 20% of the distance between olecranon and styloid process of 5th digit
(d) 20% of the distance of olecranon and acromioclavicular joint (AC) joint
(e) 40% of the distance of AC joint and olecranon
(f) 20% of the distance of AC joint to olecranon

Figure 5 shows the strain results of patient 1 for the unaffected arm in the first and second columns and for the affected arms in third and fourth columns, respectively. It is difficult to visually show the difference between GLUE and GLUE2 strain images. Therefore, to keep the paper concise, we only show the strain images of GLUE2. The windows show the location of the boxes used for calculating average strain and are placed on skin, fat and muscular regions. The location of these windows is verified by a fellowship-trained musculoskeletal radiologist (M. B.). We calculate SR for all seven patients in all 6 landmark locations, and show the results in Table II. Figure 6 visualizes the difference between strain values of unaffected and affected arms as box plots, where the strain values in Table II are used to calculate U-A for every landmark in skin, subcutaneous fat, and muscle regions. The six landmarks (from L1 to L6) are demonstrated in the horizontal axes.

Since the data cannot be assumed to have a normal Gaussian distribution, we performed the nonparametric paired Wilcoxon sign-rank test to compare the SR values of the unaffected and affected arms. The results show that SR has significantly higher values for the unaffected compared to the affected arm. Figure 6 shows that there is statistically significant difference between SR values in the affected and unaffected arms in all 6 locations in the subcutaneous fat tissue. The reason that differences in the skin (part (a)) is not as significant as fat and muscle (parts (b) & (c)) is likely because the skin layer is very thin, which can cause more variance in the SR estimates. Another reason is that this figure is only considering 7 patients, which is too small to test statistical hypothesis. To solve this problem, we consider differences at all 6 locations to increase the number of samples from 7 to $6 \times 7 = 42$, and show the results in Table III. Significant differences between the affected and unaffected arms were found for skin, subcutaneous fat and skeletal muscle SR values. The p-values for the skin, subcutaneous fat, and skeletal muscle are as follows: 1.24×10^{-5}, 1.77×10^{-8}, 8.11×10^{-7}, well below the 0.05 threshold for statistical significance. This strongly confirms the substantial difference between SR values of the unaffected and affected arms.

To compare the ratio of SR measurements at different locations, we divide the average SR values of the unaffected arm by the affected arm from Table II, and show them in Table IV. One can see that all values are more than one, meaning that SR is more in the unaffected arm. A visualization of this Table is demonstrated in Figure 7. The ratio is shown for the skin, fat, and muscle tissue types. In these seven women, the optimal location for acquiring data to distinguish the affected from the unaffected arm is the landmark 3 for the skin tissue type, landmark 2 for both subcutaneous fat and skeletal muscle area (Table IV). To obtain the overall best location, we add these three ratios at the skin, fat and muscle regions, and show the results in the last column of Table IV. The values demonstrate that locations 2, 3 and 5 have the highest difference between the two arms.

Another interesting observation from this table is that subcutis fat provides the highest difference between the SR values of the affected and unaffected arms with a very high ratio of 2.50. This is in agreement with the results of Figure 6, which showed a statistically significant difference between unaffected and affected arms for a small population of only 7 samples.

IV. DISCUSSION

The cost function of GLUE2 has two competing terms of data fidelity and continuity prior which guide the TDE towards a smooth field that also satisfies similarity of RF data. The gel pad does not have scatterers and appears dark in the B-mode image. In this region, the data term cannot guide the displacement and therefore the TDE is solely guided by the continuity prior. Window-based cross correlation methods may therefore create noisy TDEs in such regions [42]. Therefore, GLUE2 is ideally suited for the proposed study. This scenario happens also in other real-life applications such as in imaging cysts or other highly hypoechoic regions. If the gel pad contains scatterers, both data and regularization terms will guide displacement estimation and hence force normalization will likely be improved. This will be investigated in a future study.

The number of variables in the cost function is 2×10^5 for a typical RF frame of size 1000×100. Therefore, optimization of Eq. 8 entails solving a linear system with a large coefficient matrix of size $2mn \times 2mn$ given an RF frame of size $m \times n$. One of the advantage of our method is that this large coefficient matrix is a sparse matrix with nonzero elements on a diagonal band of the size $4n+1$. Therefore, the optimization step is computationally efficient.

Eq. 9 allows us to incorporate second-order derivatives of the data term into our cost function with negligible additional computational cost. If we set ϵ to a large number, we reduce the impact of the second-order derivatives. Therefore, ϵ should be set to larger values when imaging organs that generate a mostly linear data term. Our experiments corroborated this analysis and showed that higher values of ϵ are more suitable for homogenous tissues, whereas lower

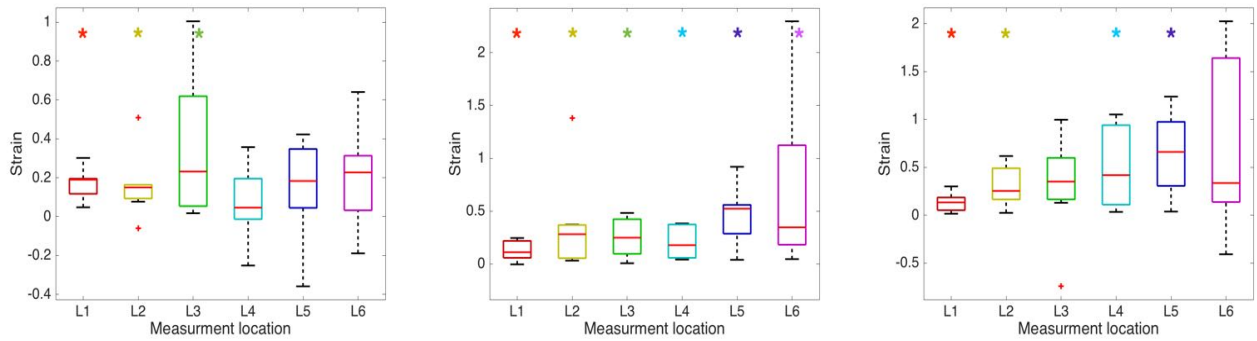

(a) Skin (b) Subcutaneous fat (c) Muscle

Fig. 6. Visual representation of Table II. The difference of strain values for unaffected and affected arms (U-A) are demonstrated as the box plots for every landmark (U: unaffected, A: affected). (a), (b), and (c) show these values for skin, fat, and skeletal muscle respectively. At each landmark L1 to L6, an asterisk * indicates significant difference ($p < 0.05$) between the affected and unaffected arms.

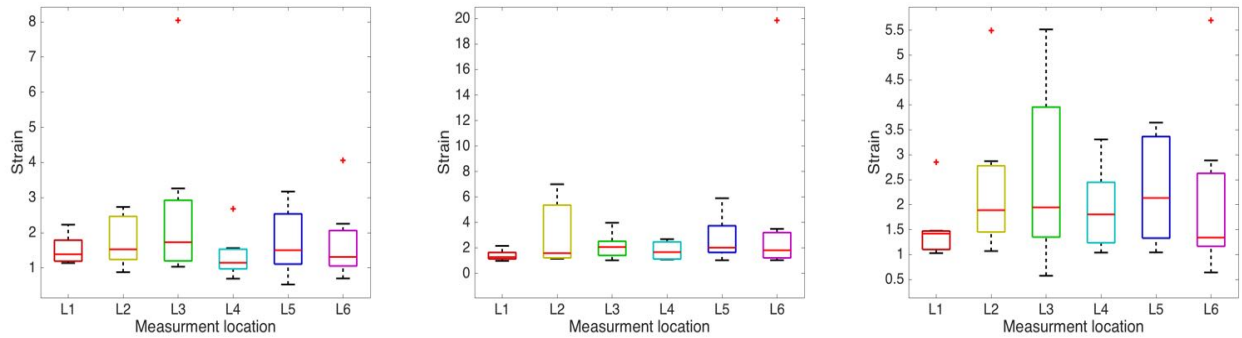

(a) Skin (b) Subcutaneous fat (c) Muscle

Fig. 7. Visual representation of Table IV. The ratio of SR values for the unaffected and affected arms (U/A) are demonstrated as the box plots for every landmark (U: unaffected, A: affected). (a), (b), and (c) show these values for skin, fat, and skeletal muscle.

values are more suitable in layered inhomogenous tissues. When a high/low value is considered regarding the tissue type (homogenous/inhomogenous) as the value of ϵ, it can be changed by 100% without noticeable difference in the results, which shows that the results are not sensitive to this parameter. Ultrasound machines often require specifying the imaging organ to load the optimized imaging parameters. The optimal value of all parameters of GLUE2, including ϵ, can be loaded in a similar fashion when imaging different organs.

The landmarks in Figure 4 are identified using a measuring tape. Therefore, the location of these landmarks in the two arms might be slightly different. Our hypothesis is that since tissue properties vary continuously, small differences in these locations do not generate large differences in strain measurements. Another limitation is that the direction of the ultrasound probe can lead to different SR measurements since tissue is anisotropic. To mitigate this, the sonographer should hold the probe perpendicular to the skin. In the future, we will estimate 3D ultrasound strain images [51], [52] to tackle these limitations of 2D imaging.

Although this study is limited to seven women with documented Stage 2 breast cancer-related lymphedema, the findings have uncovered several important and novel results that have allowed us to gain insight into the differences in tissue properties between the unaffected limb (non-lymphedematous) compared to the affected limb (lymphedematous limb). It would appear that the SR values in the affected limb are consistently and significantly lower in the skin, subcutaneous fat and skeletal muscle layers. The reduction in SR suggests a less compliant tissue when compared to a more normal or healthier tissue. This reduction was noted at every landmark location suggesting that the tissue abnormalities that are contributing to the firmer tissue properties are not specific to just a single area of the arm but can be found from the most distal (wrist) to the more proximal regions of the upper arm. Of particular interest are the lower skin SR findings in the affected compared to the unaffected limb (Table II). The pitting test has been shown to differentiate between the affected and unaffected arms in stage 3, but not always in stage 2 [53]. Our findings therefore may indicate that the proposed elastography technique is more sensitive than the pitting test. Of course, these findings are representative of only 5 women; thus more data is needed to make a more definitive conclusion.

There are several factors that can explain the overall lower SR values in the lymphedemic arm. Because of the probable inflammatory processes that are present in the affected limb, it would not be surprising that inflammatory-induced fibrotic tissue has accumulated among the tissue layers thereby causing the displacement to be less pronounced. Also, additional layering of subcutaneous fat once again brought on by localized

TABLE II
SR VALUES FOR THE LANDMARKS 1 TO 6 IN SKIN, FAT, AND MUSCULAR TISSUES (A = AFFECTED AND U = UNAFFECTED).

	Skin		Fat		Muscle	
Location 1	U	A	U	A	U	A
Patient 1	0.4469	0.2653	0.4203	0.3789	0.5848	0.3957
Patient 2	0.7946	0.6047	0.7469	0.5789	0.5479	0.5327
Patient 3	0.3565	0.3086	0.4547	0.2096	0.4619	0.1618
Patient 4	0.4323	0.2367	0.5503	0.4399	0.5732	0.4034
Patient 5	0.7747	0.6791	0.6048	0.6094	0.5717	0.5452
Patient 6	0.6918	0.4978	0.5617	0.3276	0.6157	0.4876
Patient 7	0.5467	0.2451	0.3387	0.2331	0.4273	0.2941
Average	**0.58**	**0.41**	**0.53**	**0.39**	**0.54**	**0.40**
Location 2						
Patient 1	0.2569	0.0939	0.2298	0.1984	0.3632	0.3393
Patient 2	0.4481	0.5086	0.7551	0.4741	1.104	0.6675
Patient 3	0.2949	0.1315	0.21	0.1783	0.5356	0.2834
Patient 4	0.4234	0.2832	0.4141	0.0591	0.7797	0.2714
Patient 5	0.5634	0.4866	1.654	0.2715	0.755	0.1375
Patient 6	0.8404	0.3308	0.5432	0.1707	0.4831	0.3489
Patient 7	0.4327	0.2826	0.4343	0.3141	0.4218	0.1684
Average	**0.47**	**0.30**	**0.60**	**0.24**	**0.64**	**0.32**
Location 3						
Patient 1	0.8289	0.103	0.6437	0.1616	1.2174	0.2207
Patient 2	0.6282	0.3282	0.4779	0.2299	0.5544	0.2848
Patient 3	0.5488	0.3169	0.4796	0.2509	1.0987	0.748
Patient 4	0.268	0.2427	0.1786	0.1724	0.5451	0.4156
Patient 5	0.5209	0.5038	0.6688	0.3108	1.1335	0.5181
Patient 6	1.4490	0.4443	0.7150	0.2698	1.0047	1.7480
Patient 7	0.4196	0.2802	0.2545	0.2033	0.7022	0.1544
Average	**0.67**	**0.32**	**0.49**	**0.23**	**0.89**	**0.59**
Location 4						
Patient 1	0.3601	0.3148	0.6104	0.2362	1.47	0.4441
Patient 2	0.735	0.5103	0.9173	0.5475	0.9107	0.8769
Patient 3	0.357	0.3108	0.2815	0.232	0.6512	0.6103
Patient 4	0.2983	0.1905	0.3321	0.1544	0.8401	0.4215
Patient 5	0.3757	0.4082	0.454	0.4127	1.1081	0.4258
Patient 6	0.5738	0.8255	0.8513	0.7699	2.4662	1.4151
Patient 7	0.5699	0.2125	0.6093	0.2262	0.7115	0.3941
Average	**0.47**	**0.39**	**0.58**	**0.37**	**1.16**	**0.66**
Location 5						
Patient 1	0.6451	0.5063	0.6169	0.3623	1.8268	0.5882
Patient 2	0.5168	0.3337	1.1071	0.5452	1.475	0.4045
Patient 3	0.6173	0.1945	1.0203	0.4715	2.1202	1.4337
Patient 4	0.2467	0.2333	0.4975	0.1166	0.9293	0.2691
Patient 5	0.5547	0.1935	1.1065	0.1873	0.9591	0.4493
Patient 6	0.9160	0.6077	1.3439	0.8208	0.9089	0.8714
Patient 7	0.4058	0.7646	1.0107	0.9715	1.0877	0.8498
Average	**0.56**	**0.40**	**0.95**	**0.50**	**1.32**	**0.69**
Location 6						
Patient 1	0.4075	0.1804	0.2622	0.1119	0.9612	0.805
Patient 2	0.4459	0.635	1.0297	0.9843	1.3224	0.9867
Patient 3	0.9892	0.7533	1.7792	1.2837	2.9419	1.019
Patient 4	0.3840	0.3656	0.7674	0.4212	0.9671	0.8361
Patient 5	1.0570	0.9826	1.8921	1.615	1.7234	0.9296
Patient 6	1.0357	0.6968	1.8652	0.5327	0.7279	1.1360
Patient 7	0.8505	0.2094	2.4187	0.1217	2.4554	0.4307
Average	**0.74**	**0.54**	**1.43**	**0.72**	**1.58**	**0.88**

TABLE III
RESULTS OF TABLE II SUMMARIZED FOR SKIN, FAT AND MUSCLE. SR VALUES ARE MEANS ± STANDARD DEVIATION (N=42, 7 SUBJECTS × 6 LOCATIONS FOR EACH TISSUE TYPE). P-VALUES DETERMINED USING A PAIRED WILCOXON SIGN-RANK TEST BETWEEN SUBJECTS.

Tissue	Affected Arm	Unaffected Arm	p-value
Skin	0.39±0.21	0.58±0.26	1.24×10^{-5}
Subcutaneous Fat	0.41±0.33	0.76±0.52	1.77×10^{-8}
Skeletal Muscle	0.59±0.37	1.02±0.60	8.11×10^{-7}

inflammation may also contribute to the lower SR. The change in tissue composition definitely implies an alteration in the anatomical structure that could lead to changes in functional capabilities especially with skeletal muscle function. From a clinical perspective, these findings can guide health care professionals to focus on specific target areas of the limb. These initial findings are encouraging and would direct us to evaluate how these SR values would differ among the different stages of lymphedema and from a more basic perspective, how these values differ from the limbs of healthy women.

TABLE IV
SR RATIO OF THE UNAFFECTED ARM DIVIDED BY THE AFFECTED ARM (U/A) FOR EACH LANDMARK LOCATION. AVERAGE VALUES FROM TABLE II ARE USED TO COMPUTE THESE NUMBERS. HIGHEST NUMBERS ARE HIGHLIGHTED IN BOLD FONT.

Location	Skin (Ave.) U/A	Fat (Ave.) U/A	Muscle (Ave.) U/A	Sum
1	1.41	1.35	1.35	4.11
2	1.56	**2.50**	**2.00**	**6.06**
3	**2.09**	2.13	1.51	**5.73**
4	1.21	1.57	1.76	4.54
5	1.40	1.90	1.91	**5.21**
6	1.37	1.99	1.79	5.15

V. CONCLUSIONS

In this paper, we introduced the application of quasi-static ultrasound elastography for assessment of differences between affected and unaffected arms in patients with breast cancer-related lymphedema. We proposed the biomarker of SR (Strain Ratio), and showed that it is significantly different in the affected and unaffected arms. In addition, we proposed a novel method that utilizes the second-order derivative of the data term to improve the quality of the displacement estimation. We further introduced a new time-delay estimation method that reliably estimates strain images in patient data in less than a second. Future work will focus on using the SR biomarker for staging and early diagnosis of lymphedema.

ACKNOWLEDGEMENTS

This work was supported by the Dr. Louis G. Johnson Foundation and by the Richard and Edith Strauss Canada Foundation. The authors would like to thank Z. Vajihi for her help in data collection and the women from the MUHC Lymphedema Program who participated in this study. We also thank Julian Lee from Alpinion USA for technical support.

REFERENCES

[1] A. G. Warren, H. Brorson, L. J. Borud, and S. A. Slavin, "Lymphedema: a comprehensive review," *Annals of plastic surgery*, vol. 59, no. 4, pp. 464–472, 2007.
[2] P. S. Mortimer, "The pathophysiology of lymphedema," *Cancer*, vol. 83, no. S12B, pp. 2798–2802, 1998.
[3] I. ISL, "The diagnosis and treatment of peripheral lymphedema," *Lymphology*, vol. 36, no. 2, pp. 84–91, 2003.
[4] S. G. Rockson, "Diagnosis and management of lymphatic vascular disease," *Journal of the American College of Cardiology*, vol. 52, no. 10, pp. 799–806, 2008.
[5] S. Duewell, K. D. Hagspiel, J. Zuber, G. K. von Schulthess, A. Bollinger, and W. A. Fuchs, "Swollen lower extremity: role of mr imaging." *Radiology*, vol. 184, no. 1, pp. 227–231, 1992.
[6] R. Garza, R. Skoracki, K. Hock, and S. P. Povoski, "A comprehensive overview on the surgical management of secondary lymphedema of the upper and lower extremities related to prior oncologic therapies," *BMC cancer*, vol. 17, no. 1, p. 468, 2017.
[7] A. Szuba and S. G. Rockson, "Lymphedema: classification, diagnosis and therapy," *Vascular medicine*, vol. 3, no. 2, pp. 145–156, 1998.
[8] M. Gniadecka and B. Quistorff, "Assessment of dermal water by high-frequency ultrasound: comparative studies with magnetic resonance," *British Journal of Dermatology*, vol. 135, no. 2, pp. 218–224, 1996.
[9] M. Gniadecka, "Localization of dermal edema in lipodermatosclerosis, lymphedema, and cardiac insufficiency: high-frequency ultrasound examination of intradermal echogenicity," *Journal of the American Academy of Dermatology*, vol. 35, no. 1, pp. 37–41, 1996.

[10] E. Fumiere, O. Leduc, S. Fourcade, C. Becker, C. Garbar, R. Demeure, F. Wilputte, A. Leduc, and C. Delcour, "Mr imaging, proton mr spectroscopy, ultrasonographic, histologic findings in patients with chronic lymphedema," *Lymphology*, vol. 40, no. 4, pp. 157–162, 2007.

[11] R. Righetti, B. S. Garra, L. M. Mobbs, C. M. Kraemer-Chant, J. Ophir, and T. A. Krouskop, "The feasibility of using poroelastographic techniques for distinguishing between normal and lymphedematous tissues in vivo," *Physics in Medicine & Biology*, vol. 52, no. 21, p. 6525, 2007.

[12] G. P. Berry, J. C. Bamber, P. S. Mortimer, N. L. Bush, N. R. Miller, and P. E. Barbone, "The spatio-temporal strain response of oedematous and nonoedematous tissue to sustained compression in vivo," *Ultrasound in Medicine and Biology*, vol. 34, no. 4, pp. 617–629, 2008.

[13] L. Coutts, N. Miller, P. Mortimer, and J. Bamber, "Investigation of in vivo skin stiffness anisotropy in breast cancer related lymphoedema," *Journal of biomechanics*, vol. 49, no. 1, pp. 94–99, 2016.

[14] R. H. Mellor, N. L. Bush, A. W. Stanton, J. C. Bamber, J. R. Levick, and P. S. Mortimer, "Dual-frequency ultrasound examination of skin and subcutis thickness in breast cancer-related lymphedema," *The breast journal*, vol. 10, no. 6, pp. 496–503, 2004.

[15] W. Kim, S. Chung, T. Kim, and K. Seo, "Measurement of soft tissue compliance with pressure using ultrasonography," *Lymphology*, vol. 41, no. 4, p. 167, 2008.

[16] C. Lim, H. Seo, K. Kim, S. Chung, and K. Seo, "Measurement of lymphedema using ultrasonography with the compression method," *Lymphology*, vol. 44, no. 2, p. 72, 2011.

[17] F. Hacard, L. Machet, A. Caille, V. Tauveron, G. Georgescou, I. Rapeneau, M. Samimi, F. Patat, and L. Vaillant, "Measurement of skin thickness and skin elasticity to evaluate the effectiveness of intensive decongestive treatment in patients with lymphoedema: a prospective study," *Skin Research and Technology*, vol. 20, no. 3, pp. 274–281, 2014.

[18] X. Pan, J. Gao, S. Tao, K. Liu, J. Bai, and J. Luo, "A two-step optical flow method for strain estimation in elastography: Simulation and phantom study," *Ultrasonics*, vol. 54, no. 4, pp. 990–996, 2014.

[19] H. Rivaz, E. M. Boctor, M. A. Choti, and G. D. Hager, "Ultrasound elastography using multiple images," *Medical image analysis*, vol. 18, no. 2, pp. 314–329, 2014.

[20] A. N. Ingle, C. Ma, and T. Varghese, "Ultrasonic tracking of shear waves using a particle filter," *Med. phys.*, vol. 42, no. 11, pp. 6711–6724, 2015.

[21] M. G. Kibria and M. K. Hasan, "A class of kernel based real-time elastography algorithms," *Ultrasonics*, vol. 61, pp. 88–102, 2015.

[22] J. Jiang and T. J. Hall, "A coupled subsample displacement estimation method for ultrasound-based strain elastography," *Physics in medicine and biology*, vol. 60, no. 21, p. 8347, 2015.

[23] J. Porée, D. Garcia, B. Chayer, J. Ohayon, and G. Cloutier, "Noninvasive vascular elastography with plane strain incompressibility assumption using ultrafast coherent compound plane wave imaging," *IEEE transactions on medical imaging*, vol. 34, no. 12, pp. 2618–2631, 2015.

[24] Z. Liu, C. Huang, and J. Luo, "A systematic investigation of lateral estimation using various interpolation approaches in conventional ultrasound imaging," *IEEE Transactions on Ultrasonics, Ferroelectrics, and Frequency Control*, 2017.

[25] M. S.-E. Rabbi and M. K. Hasan, "Speckle tracking and speckle content based composite strain imaging for solid and fluid filled lesions," *Ultrasonics*, vol. 74, pp. 124–139, 2017.

[26] C. Lim, B. Hwang, H. Park, D. Lee, J. Park, K. J. Lee, S. K. Kim, and K. S. Seo, "Optimal pressure for measuring objective lymphedema with postoperative ultrasonography in patients with breast cancer," *Computer Assisted Surgery*, vol. 21, no. sup1, pp. 102–110, 2016.

[27] E. Konofagou and J. Ophir, "A new elastographic method for estimation and imaging of lateral displacements, lateral strains, corrected axial strains and poisson?s ratios in tissues," *Ultrasound in Medicine and Biology*, vol. 24, no. 8, pp. 1183–1199, 1998.

[28] T. Shiina, K. R. Nightingale, M. L. Palmeri, T. J. Hall, J. C. Bamber, R. G. Barr, L. Castera, B. I. Choi, Y.-H. Chou, D. Cosgrove *et al.*, "Wfumb guidelines and recommendations for clinical use of ultrasound elastography: Part 1: basic principles and terminology," *Ultrasound in Medicine and Biology*, vol. 41, no. 5, pp. 1126–1147, 2015.

[29] R. Ahmed, R. Arfin, M. H. Rubel, K. K. Islam, C. Jia, D. Metaxas, B. S. Garra, and S. K. Alam, "Comparison of windowing effects on elastography images: Simulation, phantom and in vivo studies," *Ultrasonics*, vol. 66, pp. 140–153, 2016.

[30] M. McCormick, N. Rubert, and T. Varghese, "Bayesian regularization applied to ultrasound strain imaging," *IEEE Transactions on Biomedical Engineering*, vol. 58, no. 6, pp. 1612–1620, 2011.

[31] Z. Chen, Y. Chen, and Q. Huang, "Development of a wireless and near real-time 3d ultrasound strain imaging system," *IEEE transactions on biomedical circuits and systems*, vol. 10, no. 2, pp. 394–403, 2016.

[32] B. Byram, G. E. Trahey, and M. Palmeri, "Bayesian speckle tracking. part i: An implementable perturbation to the likelihood function for ultrasound displacement estimation," *IEEE transactions on ultrasonics, ferroelectrics, and frequency control*, vol. 60, no. 1, pp. 132–143, 2013.

[33] D. M. Dumont, K. M. Walsh, and B. C. Byram, "Improving displacement signal-to-noise ratio for low-signal radiation force elasticity imaging using bayesian techniques," *Ultrasound in Medicine and Biology*, vol. 42, no. 8, pp. 1986–1997, 2016.

[34] C. Pellot-Barakat, F. Frouin, M. F. Insana, and A. Herment, "Ultrasound elastography based on multiscale estimations of regularized displacement fields," *IEEE transactions on medical imaging*, vol. 23, no. 2, pp. 153–163, 2004.

[35] M. A. Hussain, A. J. Hodgson, and R. Abugharbieh, "Strain-initialized robust bone surface detection in 3-d ultrasound," *Ultrasound in Medicine and Biology*, vol. 43, no. 3, pp. 648–661, 2017.

[36] J. Porée, D. Posada, A. Hodzic, F. Tournoux, G. Cloutier, and D. Garcia, "High-frame-rate echocardiography using coherent compounding with doppler-based motion-compensation," *IEEE transactions on medical imaging*, vol. 35, no. 7, pp. 1647–1657, 2016.

[37] T. J Hall, P. E Barbone, A. A Oberai, J. Jiang, J.-F. Dord, S. Goenezen, and T. Fisher, "Recent results in nonlinear strain and modulus imaging," *Current medical imaging reviews*, vol. 7, no. 4, pp. 313–327, 2011.

[38] H. S. Hashemi and H. Rivaz, "Global time-delay estimation in ultrasound elastography," *IEEE Transactions on Ultrasonics, Ferroelectrics, and Frequency Control*, vol. 64, pp. 1625–1636, 2017.

[39] S. Benhimane and E. Malis, "Real-time image-based tracking of planes using efficient second-order minimization," in *Intelligent Robots and Systems, 2004.(IROS 2004). Proceedings. 2004 IEEE/RSJ International Conference on*, vol. 1. IEEE, 2004, pp. 943–948.

[40] C. Wachinger, P. Golland, C. Magnain, B. Fischl, and M. Reuter, "Multi-modal robust inverse-consistent linear registration," *Human brain mapping*, vol. 36, no. 4, pp. 1365–1380, 2015.

[41] H. Zhou and H. Rivaz, "Registration of pre-and postresection ultrasound volumes with noncorresponding regions in neurosurgery," *IEEE journal biomedical and health informatics*, vol. 20, no. 5, pp. 1240–1249, 2016.

[42] A. Nahiyan and M. K. Hasan, "Hybrid algorithm for elastography to visualize both solid and fluid-filled lesions," *Ultrasound in medicine & biology*, vol. 41, no. 4, pp. 1058–1078, 2015.

[43] H. Hashemi, S. Fallone, M. Boily, A. Towers, R. Kilgour, and H. Rivaz, "Ultrasound elastography of breast cancer-related lymphedema," in *Biomedical Imaging (ISBI 2018), 2018 IEEE 15th International Symposium on*. IEEE, 2018, pp. 1491–1495.

[44] H. Rivaz, E. M. Boctor, M. A. Choti, and G. D. Hager, "Real-time regularized ultrasound elastography," *Medical Imaging, IEEE Transactions on*, vol. 30, no. 4, pp. 928–945, 2011.

[45] S. Benhimane, A. Ladikos, V. Lepetit, and N. Navab, "Linear and quadratic subsets for template-based tracking," in *IEEE Conference Computer Vision Pattern Recognition, 2007*. IEEE, 2007, pp. 1–6.

[46] C. Mei, S. Benhimane, E. Malis, and P. Rives, "Efficient homography-based tracking and 3-d reconstruction for single-viewpoint sensors," *IEEE Transactions on Robotics*, vol. 24, no. 6, pp. 1352–1364, 2008.

[47] F. Kallel and J. Ophir, "A least-squares strain estimator for elastography," *Ultrasonic imaging*, vol. 19, no. 3, pp. 195–208, 1997.

[48] J. A. Jensen, "Field: A program for simulating ultrasound systems," in *10TH NordiBaltic Conference on Biomedical Imaging, Vol. 4, Supplementary Part 1: 351–353*. Citeseer, 1996.

[49] H. Rivaz, E. M. Boctor, and G. Fichtinger, "Ultrasound speckle detection using low order moments," in *Ultrasonics Symposium, 2006. IEEE*, 2006, pp. 2092–2095.

[50] J. Ophir, S. Alam, B. Garra, F. Kallel, E. Konofagou, T. Krouskop, and T. Varghese, "Elastography: ultrasonic estimation and imaging of the elastic properties of tissues," *Proceedings of the Institution of Mechanical Engineers, Part H: Journal of Engineering in Medicine*, vol. 213, no. 3, pp. 203–233, 1999.

[51] H. Rivaz, I. Fleming, L. Assumpcao, G. Fichtinger, U. Hamper, M. Choti, G. Hager, and E. Boctor, "Ablation monitoring with elastography: 2d in-vivo and 3d ex-vivo studies," *Medical Image Computing and Computer-Assisted Intervention–MICCAI 2008*, pp. 458–466, 2008.

[52] A. Ingle, T. Varghese, and W. A. Sethares, "Efficient 3-d reconstruction in ultrasound elastography via a sparse iteration based on markov random fields," *IEEE transactions on ultrasonics, ferroelectrics, and frequency control*, vol. 64, no. 3, pp. 491–499, 2017.

[53] K. Levenhagen, C. Davies, M. Perdomo, K. Ryans, and L. Gilchrist, "Diagnosis of upper-quadrant lymphedema secondary to cancer: Clinical practice guideline from the oncology section of apta," *Rehabilitation Oncology (American Physical Therapy Association. Oncology Section)*, vol. 35, no. 3, p. E1, 2017.